Aerospace Science and Technology 124 (2022) 107528

Contents lists available at ScienceDirect

Aerospace Science and Technology

www.elsevier.com/locate/aescte

Active disturbance rejection controllers optimized via adaptive granularity learning distributed pigeon-inspired optimization for autonomous aerial refueling hose-drogue system

Yongbin Sun, Zhijie Liu, Yao Zou *, Xiuyu He

School of Automation and Electrical Engineering, University of Science and Technology Beijing, Beijing 100083, China

ARTICLE INFO

Article history:
Received 10 October 2021
Received in revised form 21 March 2022
Accepted 29 March 2022
Available online 1 April 2022
Communicated by Qiulin Qu

Keywords:
Autonomous aerial refueling (AAR)
Hose-drogue system (HDS)
Optimized drogue active disturbance rejection controller
Adaptive granularity learning distributed pigeon-inspired optimization (AGLDPIO)

ABSTRACT

The autonomous aerial refueling (AAR) hose-drogue system (HDS) suffers the multi-wind disturbances leading to the low stability of drogue position, which is adverse for the successful probe-and-drogue AAR docking. This paper addresses the drogue position stability control problem in the presence of multi-wind disturbances. The finite-segment multi-body method is adopted to model the hose-drogue assembly as a link-connected system. A controllable drogue is equipped at the end of the hose to stabilize the drogue's relative position in the presence of tanker trailing vortex, receiver bow wave, atmospheric turbulence, and gust. Thus, the drogue active disturbance rejection controllers (ADRC) are designed to enhance the anti-disturbance ability and position stability of HDS. Besides, an improved pigeon-inspired optimization (PIO), adaptive granularity learning distributed PIO (AGLDPIO), is proposed to optimize the drogue lateral and vertical position controllers for realizing the optimal control effects and reducing the difficulties of parameter tuning. The simulation results show that the proposed optimized ADRC position controllers can effectively maintain the drogue swinging in a smaller range, which demonstrates the effectiveness and superiority of the proposed controllers.

1. Introduction

Recently, unmanned aerial vehicles (UAVs) [1,2] have attracted much attentions due to their crucial applications in cooperative search [3,4], surveillance [5], target tracking [6], cooperative attack [7], etc. However, the inevitable conflict between the UAV payload and endurance limits the combat effectiveness of UAVs. Autonomous aerial refueling (AAR) [8,9] is known as an effective method to deal with this conflict as declared in Unmanned Aircraft Systems Roadmap 2005-2030 [10], which can increase the autonomy of UAVs. In general, there are three widely applicated aerial refueling approaches: the boom-receptacle refueling (BRR) [11], the probe-and-drogue refueling (PDR) [12,13], and the boom drogue adapter units refueling [13]. In comparison with the other two approaches, the PDR performs better in certain aspects, such as the flexible refueling hold position, multi-UAVs simultaneous refueling, helicopter refueling, partner refueling, etc. Thus, the PDR is adopted as the main aerial refueling approach worldwide, especially for UAVs. In this paper, we mainly focus on the probe-and-drogue AAR technique of UAVs.

Due to the flexibility of hose, the hose-drogue assembly suffers the adverse influences of the tanker trailing vortex, receiver bow wave, atmospheric turbulence, and gust in the AAR docking. To be specific, the intensities of tanker trailing vortex and receiver bow wave are related to the relative positions between the tanker and receiver UAVs. In the last few meters of docking, the receiver bow wave appears a dramatic change causing a huge position change of drogue in a short time. The atmospheric turbulence induces the drogue swinging randomly, which increases the uncertainty of docking into an experiential or predetermined stable position of drogue. Therefore, it is essential to design a drogue active disturbance rejection control method to stabilize the drogue position inside the effective range of successful docking.

To explore the dynamic and kinematic properties of the hose-drogue system (HDS), many research institutions and scholars have conducted substantial simulations and experiments. NASA Dryden Flight Research Center [14,15] took a lot of wind tunnel and outfield

* Corresponding author.
E-mail address: zouyao@ustb.edu.cn (Y. Zou).

https://doi.org/10.1016/j.ast.2022.107528
1270-9638/

flight tests such that the abundant aerodynamic data of the HDS was gathered for analyzing and modeling its dynamics. A wing-pod refueling hose model was built by the Boeing Company [16] to depict the dynamic properties of the hose. Besides, Zhu and Meguid [17] modeled the HDS using the finite element method with an accurate and computationally efficient curved beam element, and studied its dynamic characteristics and stability. In [18], the dynamic model of hose-drogue assembly was established via the finite-segment method, and the dynamic properties of drogue were investigated under the influence of atmospheric turbulence and tanker maneuver. Moreover, a pendulum-based hose model was developed in [19], and further Williamson et al. modeled the aerodynamics of controllable drogue that could control the aerodynamic forces through changing the drogue's canopy. In addition, Wang et al. [20] proposed a variable-length hose-drogue model and developed a sliding model backstepping controller to restrain the hose whipping phenomenon (HWP). Liu et al. [21,22] modeled the flexible hose as a distributed parameter system described by partial differential equations (PDEs) and devised the boundary control schemes to dampen the flexible hose's vibration in the presence of varying length, varying speed and input constraint. As mentioned above, the related works about the HDS mainly focus on the model and dynamic characteristics of hose-drogue assembly. For the hose-drum unit, the sliding model backstepping controller in [20] was designed to maintain the hose tension by reeling in/out the hose during the probe-drogue coupling, which was applied to deal with the hose whipping problem caused by the redundant hose length. In terms of the receiver UAV, the slow-dynamic receiver UAV is difficult to track the fast-dynamic drogue in principle [13] under the influence of multi-wind disturbances, and even if the predictive position compensation strategy [12] is developed to handle this problem, there is still a certain probability of docking failure due to the time-varying wind disturbances and the imperfect strategy. Compared with the two above-mentioned control schemes, the more direct control scheme, i.e., the drogue position control scheme, is a supplementary scheme to enhance the docking success rate except for the receiver UAV control scheme. It can more effectively stabilize the drogue in a smaller swing range with a faster response speed. In essence, the drogue control scheme transforms the dynamic target tracking problem to the static relative position control problem, which can greatly reduce the difficulty of the original problem. It is worth noting that the drogue's electricity-leakage protection for the sensors and control unit must be considered in particular before the practical application. Thus, in the pre-docking stage, the effective active disturbance rejection control method for the drogue should be designed to stabilize the relative positions in the presence of multi-wind disturbances.

Hitherto, only few control methods have been proposed for designing the drogue position controller. Among them, the proportion-integration-differentiation (PID) method is commonly adopted for designing the drogue control law as presented in [23]. Although the physical meaning and form of the PID controller are explicit, the insufficient stability of drogue position controller could be induced by the abrupt changes of multi-wind disturbances in the docking. The linear quadratic regulator (LQR) method [24,25] is also applied for the controller design. However, the HDS model presents the ultra high degrees of freedom and the strong nonlinearity, and it is almost impossible to measure all the feedback control states used for the drogue LQR controller design. In our previous paper [26], the fractional-order control theory is adopted to design the optimized fractional-order PID (FOPID) controllers for the HDS. Though the FOPID controller performs better than PID controller in the stability of drogue position control, the characteristics of multi-wind disturbances are ignored in the design process of drogue position controller. Consequently, the optimized FOPID controllers in [26] have the insufficient ability to resist the multi-wind disturbances, especially for the abrupt change of receiver bow wave. Therefore, in this paper, we develop the active disturbance rejection controllers (ADRC) to increase the anti-disturbance ability and position stability of drogue. Besides, an improved evolutionary algorithm is proposed to optimize the capability of the drogue ADRC controllers and reduce the workload of designers.

Traditional evolutionary algorithms (EAs), including particle swarm optimization (PSO) [27], ant colony optimization (ACO) [28], artificial bee colony (ABC) algorithm [29], brain storm optimization (BSO) [30], etc., have attracted much attentions in the applications of the practical scientific problems. Duan et al. [31] firstly proposed a novel swarm intelligence optimization algorithm called pigeon-inspired optimization (PIO) for path planning. Further, the UAV target detection problem was handled by Li and Duan [32] through an improved PIO and the edge potential function. In [33], an obstacle avoidance control method for multiple UAVs was proposed on the basis of the multi-objective social learning PIO. Besides, a dynamic discrete PIO algorithm [7] was developed to accomplish the multi-UAV cooperative search-attack mission planning. In [34], Alazzam et al. proposed a feature selection algorithm for intrusion detection system based on PIO. In this paper, the adaptive granularity learning strategy (AGLS) based on the locality-sensitive hashing (LSH) and the logistic regression (LR) [35] is introduced into the master-slave multisubpopulation distributed PIO (AGLDPIO) for enhancing the swarm population diversity, which determines an appropriate subpopulation size to balance the exploration and exploitation abilities.

In this paper, an optimized drogue active disturbance rejection control method is proposed for autonomous aerial refueling hose-drogue system. To describe the flexibility of HDS, a finite-segment multi-body dynamic model with a controllable drogue is built for the control law design of HDS. The AAR atmospheric flow environment is simulated by incorporating the tanker trailing vortex, receiver bow wave, atmospheric turbulence, and gust. Then, the lateral and vertical ADRC position controllers are designed to enhance the drogue's stability in the presence of multi-wind disturbances. Furthermore, the AGLDPIO algorithm is developed to optimize the designed ADRC position controllers such that the controllers can realize the relatively optimal control effects with respects to the control accuracy, response speed, and anti-disturbance ability.

The rest of the paper is organized as follows. Section 2 presents the models of the HDS and multi-wind disturbances. The adaptive granularity learning distributed PIO algorithm is given in Section 3. In Section 4, the optimized active disturbance rejection controllers are designed to stabilize the lateral and vertical positions of drogue. Then, the simulation results are shown and discussed in Section 5. Finally, Section 6 concludes the paper.

2. Hose-drogue assembly and multi-wind disturbance modeling

2.1. Modeling assumptions and coordinate frame definition

Throughout this paper, $\mathbb{R}$ denotes a real number set, $\mathbb{R}^{m\times n}$ denotes a real matrix of dimension $m \times n$.

To describe the flexibility of HDS, the hose-drogue assembly is attempted to model as a link-connected system. For simplification, we make some modeling assumptions as follows:

1) The hose is constituted by a certain number of links that are connected with frictionless joints.

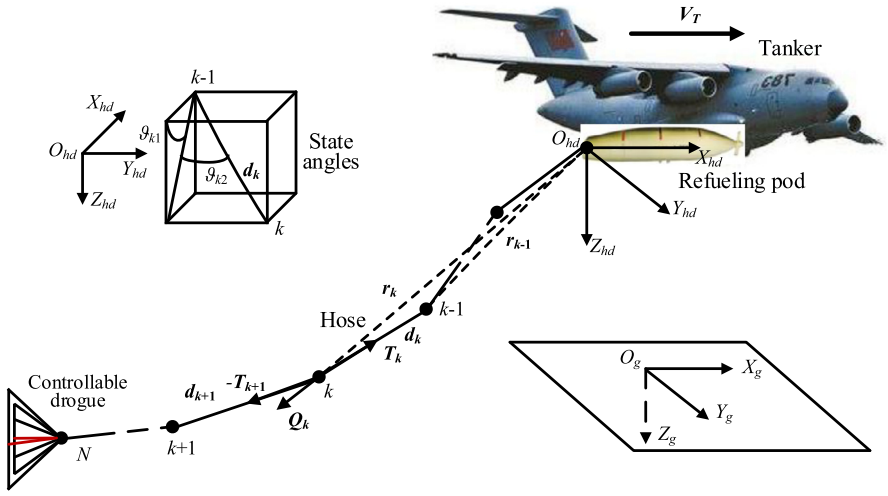

Fig. 1. Hose-drogue assembly and related coordinate frames.

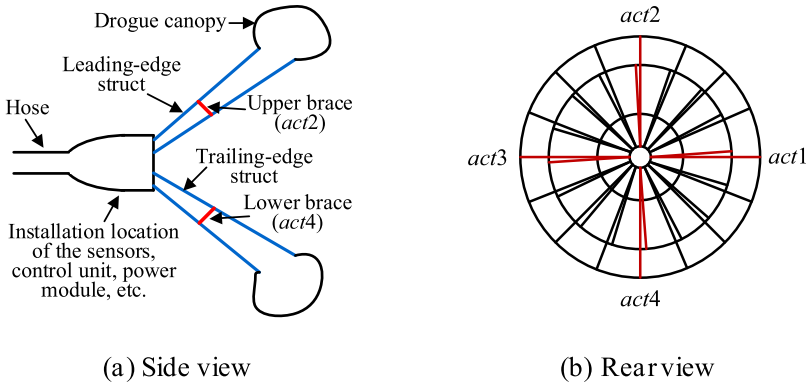

Fig. 2. Controllable drogue.

2) Based on the lumped parameter method, the aerodynamic forces and mass are concentrated on the frictionless joints.
3) The twist, elasticity, and damping of the hose-drogue assembly are ignored.

The HDS mainly contains three parts: the hose, the controllable drogue [19], and the state sensors. Fig. 1 presents the hose-drogue assembly and the related coordinate frames. The hose-drogue assembly is modeled in the traction point coordinate frame $O_{hd}X_{hd}Y_{hd}Z_{hd}$ that is parallel to the tanker-body coordinate frame. $O_gX_gY_gZ_g$ denotes the inertial coordinate frame. We define two state angles of the hose's k-th link as $\vartheta_{k1}, \vartheta_{k2}$ which are respectively the included angles relative to the planes $O_{hd}X_{hd}Y_{hd}$ and $O_{hd}X_{hd}Z_{hd}$. The hose tensions $\boldsymbol{T}_{k-1}, \boldsymbol{T}_k \in \mathbb{R}^{3\times1}$, the hose equivalent restoring force $\boldsymbol{R}_k \in \mathbb{R}^{3\times1}$, the gravity and the aerodynamic forces are acting on the k-th lumped mass. As shown in Fig. 2, the drogue controllable actuators respectively locate at the starboard brace (actuator 1), the port-side brace (actuator 3), the upper brace (actuator 2), and the lower brace (actuator 4). The diagonal actuators are aligned with the horizontal and vertical lines, respectively. The sensors, control unit, power module, etc. are equipped at the joint location of the hose and the drogue.

2.2. Hose-drogue assembly modeling

The finite-segment multi-body method is adopted to model the hose-drogue assembly as a link-connected system [18,20]. To stabilize the drogue relative position in the presence of multi-wind disturbances, we focus on the drogue's aerodynamic forces changing with the opening angles of actuators.

The drogue's resultant external force $\boldsymbol{Q}_{dro} \in \mathbb{R}^{3\times1}$ contains the gravity and the aerodynamic forces, which is presented as [18]

$$\boldsymbol{Q}_{dro} = \left(\frac{m_N}{2} + m_{dro}\right)\boldsymbol{g} + \frac{\boldsymbol{D}_N}{2} + \boldsymbol{D}_{dro} \tag{1}$$

where m_N, m_{dro} are the mass of the hose's N-th link and the controllable drogue, respectively, g is the gravitational acceleration, $\boldsymbol{g} = [0, 0, g]^T$, $\boldsymbol{D}_N \in \mathbb{R}^{3\times1}$ denotes the aerodynamic force of the hose's N-th link, which is obtained as described in [18,20], $\boldsymbol{D}_{dro} \in \mathbb{R}^{3\times1}$ is the aerodynamic force of drogue. $\boldsymbol{D}_{dro}$ can be equivalently decomposed into two parts: the original force and the additional force. To be specific, the original force is positively correlated with the drogue's airspeed. The additional force is generated through changing the opening angles $(u_{act1}, u_{act2}, u_{act3}, u_{act4})$ of drogue's struct-braces, which can reduce the swinging range of drogue. Thus, we formulate the aerodynamic force $\boldsymbol{D}_{dro}$ as

$$\boldsymbol{D}_{dro} = -\frac{1}{2}\rho\|\boldsymbol{V}_{N,air}\|\left(\frac{\pi d_{dro}^2}{4}\right)c_{dro}\boldsymbol{V}_{N,air} + \boldsymbol{F}'_D \tag{2}$$

where ρ denotes the local air density, $\boldsymbol{V}_{N,air} \in \mathbb{R}^{3\times1}$ is the airspeed of the N-th lumped mass, $\boldsymbol{V}_{N,air} = \boldsymbol{V}_N - \boldsymbol{V}_w$, $\boldsymbol{V}_N \in \mathbb{R}^{3\times1}$ is the ground velocity of the N-th lumped mass, $\boldsymbol{V}_w \in \mathbb{R}^{3\times1}$ is the local synthetic wind velocity of multi-wind disturbances, d_{dro} is the drogue diameter, c_{dro} denotes the aerodynamic force coefficient of drogue, $\boldsymbol{F}'_D \in \mathbb{R}^{3\times1}$ is the real additional force, which are also called as the real active-control aerodynamic force. Assuming that the expected active-control aerodynamic force obtained by the designed controllers is denoted as $\boldsymbol{F}_D = \begin{bmatrix} 0 & F_s & F_v \end{bmatrix}^T$, F_s, F_v are the expected lateral and vertical forces, respectively. $\boldsymbol{F}'_D = \begin{bmatrix} F'_h & F'_s & F'_v \end{bmatrix}^T$ is calculated as [19]

$$\boldsymbol{F}'_D = \frac{1}{2}\rho\|\boldsymbol{V}_{N,air}\|^2\boldsymbol{C}_u(\boldsymbol{u}_{act} - \boldsymbol{u}_0) \tag{3}$$

where $\boldsymbol{C}_u \in \mathbb{R}^{3\times4}$ is the drogue's opening angular aerodynamic coefficient, $\boldsymbol{u}_{act} \in \mathbb{R}^{4\times1}$ denotes the real opening angle of actuator, $\boldsymbol{u}_{act} = [u_{act1}, u_{act2}, u_{act3}, u_{act4}]^T$, $\boldsymbol{u}_0 \in \mathbb{R}^{4\times1}$ is the actuator trim opening angle under a certain flight condition, $\boldsymbol{u}_0 = [u_{act1}^{trim}, u_{act2}^{trim}, u_{act3}^{trim}, u_{act4}^{trim}]^T$, F'_h, F'_s, F'_v are the real forward, lateral, and vertical active-control aerodynamic forces, respectively. According to the wind-tunnel test results [19], the controllable drogue would generate a positive lateral force with decreasing u_{act1} and increasing u_{act3}, and generate a positive vertical force with decreasing u_{act2} and increasing u_{act4}. Note that the roll angle of drogue is tiny due to the high speed flight of tanker. When the horizontal (u_{act1} and u_{act3}) or vertical (u_{act2} and u_{act4}) actuators change the opposite angle, F'_h would be approximate to zero in that the diagonal actuators have the opposite aerodynamic effect. Further, considering the actuator dynamic process, the transfer function of actuator is presented as

$$\frac{u_{out}}{u_{in}} = \frac{20}{s+20} \tag{4}$$

2.3. Multi-wind disturbance modeling

The multi-wind disturbances mainly include the tanker trailing vortex, receiver bow wave, atmospheric turbulence, and gust, which are modeled to construct the AAR atmospheric flow environment.

2.3.1. Tanker trailing vortex

The Hallock-Burnham model [36] is adopted to describe the characteristics of tanker trailing vortex due to the high precision and easy implementation. It is worth noting that the center of tanker trailing vortex tends to move down, and its radius diffuses along with the generation time. Thus, the improved Hallock-Burnham model is presented as [24]

$$V_{vory} = \frac{\Gamma_0}{2\pi}\left[\frac{z'_{rel}}{(y'_{rel} - \pi b_T/8)^2 + r_c'^2 + z'^2_{rel}} - \frac{z'_{rel}}{(y'_{rel} + \pi b_T/8)^2 + r_c'^2 + z'^2_{rel}}\right] \tag{5}$$

$$V_{vorz} = \frac{\Gamma_0}{2\pi}\left[\frac{y'_{rel} + \pi b_T/8}{(y'_{rel} + \pi b_T/8)^2 + r_c'^2 + z'^2_{rel}} - \frac{y'_{rel} - \pi b_T/8}{(y'_{rel} - \pi b_T/8)^2 + r_c'^2 + z'^2_{rel}}\right] \tag{6}$$

where V_{vorx}, V_{vory}, V_{vorz} are the wind velocity components in x, y, z-axes, respectively, $V_{vorx} \approx 0$ according to the model property, Γ_0 denotes the initial intensity of trailing vortex, $\Gamma_0 = 4G_T/(\pi\rho V_T b_T)$, G_T, V_T are the tanker gravity and velocity, respectively, $G_T = m_T g$, b_T is the tanker wingspan, $\begin{pmatrix} x'_{rel} & y'_{rel} & z'_{rel} \end{pmatrix}$ is the improved coordinates, $x'_{rel} = x^T_{rel} + d_x$, $y'_{rel} = y^T_{rel}$, $z'_{rel} = z^T_{rel} + d_z + V_{mz}(x'_{rel}/V_T)$, $\begin{pmatrix} d_x & 0 & d_z \end{pmatrix}$ is the offset value between the trailing vortex coordinate frame $O_{TV}X_{TV}Y_{TV}Z_{TV}$ and tanker-body coordinate frame $O_{TB}X_{TB}Y_{TB}Z_{TB}$, $\begin{pmatrix} x^T_{rel} & y^T_{rel} & z^T_{rel} \end{pmatrix}$ is the coordinates of one point of trailing vortex field in $O_{TB}X_{TB}Y_{TB}Z_{TB}$, V_{mz} denotes the downward velocity of trailing vortex, $V_{mz} = 2\Gamma_0/(\pi^2 b_T)$, r'_c is the improved radius of trailing vortex, $r'_c = 0.5\sqrt{-(x_{rel} + d_x)/V_T}$.

2.3.2. Receiver bow wave

In the AAR docking, the drogue tends to move away from the receiver nose along with the approaching maneuver. Especially in the last few meters of docking, the receiver bow wave's up-wash effect induces the drogue move to outward and upward directions in a short time, which is possible to cause the AAR accidents. In this paper, one half of an ellipsoid is adopted as the typical receiver nose, and the probe is equipped at the right side of the receiver nose. The Rankine half body model [37] is built to reflect the receiver bow wave effect for the hose-drogue assembly. The wind velocity components of bow wave in x, y, z-axes (i.e., $\begin{bmatrix} V_{bowx} & V_{bowy} & V_{bowz} \end{bmatrix}$) are calculated as [24]

$$V_{bowx} = v_r\cos\theta - v_\theta\sin\theta \tag{7}$$

$$V_{bowy} = (v_r\sin\theta + v_\theta\cos\theta)\frac{y_{bw}^2}{\sqrt{y_{bw}^2 + z_{bw}^2}} \tag{8}$$

$$V_{bowz} = (v_r\sin\theta + v_\theta\cos\theta)\frac{z_{bw}^2}{\sqrt{y_{bw}^2 + z_{bw}^2}} \tag{9}$$

where $\begin{pmatrix} x_{bw} & y_{bw} & z_{bw} \end{pmatrix}$ denotes the coordinate position in bow wave coordinate frame $O_{BW}X_{BW}Y_{BW}Z_{BW}$, θ is the polar angle in bow wave polar coordinate frame, v_r, v_θ are respectively the radial velocity and circumferential velocity in polar coordinate frame, which are computed as

$$v_r = U\cos\theta + \frac{Q_b}{2\pi r} \tag{10}$$

$$v_\theta = -U\sin\theta \tag{11}$$

where U is the averaged flow velocity, Q_b is the intensity of point source flow, $Q_b = 2\pi U b_n$, $b_n = h_{nose}/\pi$, h_{nose} denotes the maximum radius of receiver nose in width direction, r is the polar radius in polar coordinate frame.

2.3.3. Atmospheric turbulence and gust

The atmospheric turbulence results in the high frequency irregular swinging of drogue, and the gust induce the momentary position mutation of drogue. In this paper, the continuous Dryden turbulence model [38] in MIL-F-8785C is implemented to describe the atmospheric turbulence. Besides, we adopt a step function as the gust model.

3. Adaptive granularity learning distributed PIO algorithm

3.1. PIO algorithm

Inspired by the pigeon navigation mechanism in the long and close distances, Duan et al. [31] firstly propose the PIO algorithm that contains the map and compass operator, and the landmark operator. The two operators respectively simulate the sun and magnetic field navigation in the long distance, and the visual landmark navigation in the close distance of homing pigeons. The homing behaviors of pigeons (i.e., the two operators) can be regarded as the processes where the potential solutions search and converge to the optimal solution.

(1) Map and compass operator:

For a D-dimension search space, we define the velocity and position of the i-th pigeon at the Nc-th generation as $\boldsymbol{V}_i^{Nc} = [v_{i1}^{Nc}, v_{i2}^{Nc}, \cdots, v_{iD}^{Nc}]$, $\boldsymbol{X}_i^{Nc} = [x_{i1}^{Nc}, x_{i2}^{Nc}, \cdots, x_{iD}^{Nc}]$, respectively. The new velocity and position of the i-th pigeon at the Nc-th generation are updated as [24,29]

$$\boldsymbol{V}_i^{Nc} = e^{-R\cdot Nc}\cdot \boldsymbol{V}_i^{Nc-1} + rand\cdot\left(\boldsymbol{X}_{gbest} - \boldsymbol{X}_i^{Nc-1}\right) \tag{12}$$

$$\boldsymbol{X}_i^{Nc} = \boldsymbol{X}_i^{Nc-1} + \boldsymbol{V}_i^{Nc} \tag{13}$$

where $\boldsymbol{X}_{gbest}$ denotes the current global best position of pigeons, $\boldsymbol{X}_{gbest} = [x_{g1}, x_{g2}, \cdots, x_{gD}]$, N_p is the number of pigeons, $i = 1, 2, \cdots, N_p$, R is the map and compass factor, $rand$ is a rand number, $rand \in [0, 1]$.

(2) Landmark operator:

In the processes of the visual landmark navigation of pigeons, half of the pigeons familiar with the landmarks are chosen as the experienced ones, and the other half of the pigeons are eliminated. At the next generation, the positions of pigeons would be updated through following the center of the remaining pigeons. Thus, the position of the i-th pigeon at the Nc-th generation is calculated as [26,31]

$$N_p^{Nc} = \left\lceil \frac{N_p^{Nc-1}}{2} \right\rceil \tag{14}$$

$$\boldsymbol{X}_c^{Nc-1} = \frac{\sum_{i=1}^{N_p^{Nc-1}} \boldsymbol{X}_i^{Nc-1}\cdot fitness(\boldsymbol{X}_i^{Nc-1})}{\sum_{i=1}^{N_p^{Nc-1}} fitness(\boldsymbol{X}_i^{Nc-1})} \tag{15}$$

$$\boldsymbol{X}_i^{Nc} = \boldsymbol{X}_i^{Nc-1} + rand\cdot\left(\boldsymbol{X}_c^{Nc-1} - \boldsymbol{X}_i^{Nc-1}\right) \tag{16}$$

where $\lceil\cdot\rceil$ denotes the ceil value of number, N_p^{Nc}, N_p^{Nc-1} are the numbers of pigeons at the Nc-th and Nc-1-th generations, respectively, $\boldsymbol{X}_c^{Nc-1}$ is the center of pigeons at the Nc-1-th generation, $fitness(\cdot)$ denotes the fitness function, which is adopted as the sum of squares of the drogue's position errors. In this paper, we minimize the fitness function to optimize the drogue ADRC controllers.

3.2. AGLDPIO algorithm

The adaptive granularity learning strategy is introduced into the master-slave multisubpopulation distributed PIO, called as AGLDPIO, to enhance the swarm population diversity of PIO. In the evolution process, the master node divides the entire population into N_p/M subpopulations (i.e., the slave nodes), where M denotes the population size of slave node. If $N_p\%M \neq 0$, the last slave node would have $M + N_p\%M$ pigeons, where % presents the modulo operation. The master node dominates the multiple slave nodes in the parallel evolution. Besides, the number of slave nodes is adaptively adjusted in that the population size of slave node is adaptively controlled based on the LSH and LR, which can balance the exploration and exploitation abilities of the entire population of pigeons.

(1) Improved map and compass operator:

In each subpopulation, only the worst pigeon $\boldsymbol{X}_w$ needs to be updated through learning from the best pigeon in current subpopulation (i.e., subpopulation best notated as $\boldsymbol{X}_{sbest}$) and the best pigeon in entire population (i.e., global best notated as $\boldsymbol{X}_{gbest}$). The other pigeons in current subpopulation would directly enter to the next generation. The mentioned update operators in AGLDPIO are helpful to prolong

the evolution process for increasing the solution accuracy and saving the computation complexity. Thus, the velocity $\boldsymbol{V}_{wj}^{Nc}$ and position $\boldsymbol{X}_{wj}^{Nc}$ of the worst pigeon in each subpopulation at the Nc-th generation are updated as

$$\boldsymbol{V}_{wj}^{Nc} = e^{-R\cdot Nc}\cdot \boldsymbol{V}_{wj}^{Nc-1} + rand_1\cdot\left(\boldsymbol{X}_{sbest} - \boldsymbol{X}_{wj}^{Nc-1}\right) + rand_2\cdot\left(\boldsymbol{X}_{gbest} - \boldsymbol{X}_{wj}^{Nc-1}\right) \tag{17}$$

$$\boldsymbol{X}_{wj}^{Nc} = \boldsymbol{X}_{wj}^{Nc-1} + \boldsymbol{V}_{wj}^{Nc} \tag{18}$$

where $j = 1, 2, \cdots, N_p/M$, $rand_1$, $rand_2$ are two random numbers, $rand_1 \in [0, 1]$, $rand_2 \in [0, 1]$. The subpopulation size M affects the learning granularity of pigeons in each subpopulation, and further affects the swarm diversity for exploration and the convergence for exploitation. A large subpopulation size M means that the worst pigeon $\boldsymbol{X}_w$ learns from a large neighborhood, which is beneficial for accelerating the convergence of algorithm. Conversely, a small subpopulation size M represents that $\boldsymbol{X}_w$ learns from a small neighborhood (i.e., the number of subpopulations is large) so that more subpopulation bests $\boldsymbol{X}_{sbest}$ are helpful to increase the swarm diversity of pigeons. To precisely determine a suitable M in different evolution states, the clustering analysis method based on LSH and the adaptive granularity control based on LR are introduced into AGLDPIO for adaptively adjusting the subpopulation size M.

For each pigeon $\boldsymbol{X}_i^{Nc} = [x_{i1}^{Nc}, x_{i2}^{Nc}, \cdots, x_{iD}^{Nc}]$, first randomly generate a D-dimension vector $\boldsymbol{O}$ in the search space, $\boldsymbol{O} = [o_{i1}, o_{i2}, \cdots, o_{iD}]$, then calculate the dot product $\boldsymbol{X}_i^{Nc}\boldsymbol{O}^T$ which projects the pigeon $\boldsymbol{X}_i^{Nc}$ onto a line. If two pigeons $\boldsymbol{X}_1^{Nc}$ and $\boldsymbol{X}_2^{Nc}$ are close (i.e., $\|\boldsymbol{X}_1^{Nc} - \boldsymbol{X}_2^{Nc}\|$ is small), the projection distance $(\boldsymbol{X}_1^{Nc} - \boldsymbol{X}_2^{Nc})\boldsymbol{O}^T$ is also small with a large probability such that they are very likely in a same bucket. In contrast, a large projection distance means that the two pigeons $\boldsymbol{X}_1^{Nc}$ and $\boldsymbol{X}_2^{Nc}$ are in the same bucket with a small probability. Assuming the maximum and minimum projection coordinates of all the pigeons are $h_{\max}$ and $h_{\min}$, respectively. Then, the projection bucket size r_b is formulated as

$$r_b = \frac{h_{\max} - h_{\min}}{n_b} \tag{19}$$

where n_b denotes the bucket number. Thus, the hash line is divided into n_b equal-width buckets with size r_b, and all the pigeons are projected to the corresponding hash values. The pigeons in the same bucket are distributed to the same cluster.

When much more pigeons cluster nearby the global worst $\boldsymbol{X}_{gworst}$ than the global best $\boldsymbol{X}_{gbest}$, a smaller M or decreasing M can result in a larger number of subpopulations to improve the population diversity of the exploration state, which is helpful to escape from the local optimum. In contrast, if much more pigeons cluster nearby the $\boldsymbol{X}_{gbest}$ than the $\boldsymbol{X}_{gworst}$, a larger M or increasing M can increase the learning neighborhood of the current pigeon for accelerating the convergence of the exploitation state. According to the machine learning mechanism, the LR is an effective binary classifier to determine whether the algorithm is in the exploration or exploitation states. The subpopulation size M is adaptively adjusted at the beginning of every generation as

$$M = M - \text{round}\big(f(N_{gworst} - N_{gbest})\big) \tag{20}$$

where N_{gworst}, N_{gbest} denote the number of pigeons in the same cluster with $\boldsymbol{X}_{gworst}$ and $\boldsymbol{X}_{gbest}$, respectively, $f(\cdot)$ is the function that maps the input variables to a probability range, which is adopted as the *Tanh-sigmoid* function as

$$f(n) = \frac{1 - e^{-2n}}{1 + e^{-2n}} \tag{21}$$

Thus, if $N_{gworst} \gg N_{gbest}$, the subpopulation size M would decrease by 1 to improve the population diversity, and if $N_{gbest} \gg N_{gworst}$, M would increase by 1 to speed up the convergence, and if $N_{gbest} \approx N_{gworst}$, M would keep unchanged, which means that the current population size has a good balance between the swarm diversity and the convergence.

(2) The improved landmark operator is the same as the landmark operator of the PIO algorithm.

4. Optimized active disturbance rejection controllers

4.1. Drogue ADRC position controller design

The main purpose of the drogue position controller is resisting the adverse impacts of multi-wind disturbances for drogue stability. In contrast to the drogue PID and FOPID controllers in [23,26], the ADRC method [39] takes into account of the characteristics of multi-wind disturbances in the design process of the drogue position controllers, which can significantly enhance the anti-disturbance ability of controllers.

The ADRC controller generally contains the tracking differentiator (TD), the extended state observer (ESO), and nonlinear state error feedback (NLSEF). In this paper, the TD is removed in that the drogue stable position command remains unchanged in the AAR docking. The following assumptions are given before designing the drogue ADRC controllers.

Assumption 1. The real-time positions of drogue can be obtained through the direct or indirect measurement means. The drogue's position sensors can be adopted as the differential global positioning system (DGPS), or the photoelectric camera, or the laser.

Assumption 2. The lumped disturbances including the model uncertainties and multi-wind disturbances are differentiable, and the differentials are bounded.

Then, the ESOs of the drogue lateral and vertical controllers are constructed based on Assumptions 1-2, which are formulated as

$$\begin{cases} \dot{\widehat{\boldsymbol{P}}}_{dro} = \widehat{\boldsymbol{H}}_{dro} + \boldsymbol{\lambda}_{dro1}(\boldsymbol{P}_{dro} - \widehat{\boldsymbol{P}}_{dro}) \\ \dot{\widehat{\boldsymbol{H}}}_{dro} = \boldsymbol{\lambda}_{dro2}(\boldsymbol{P}_{dro} - \widehat{\boldsymbol{P}}_{dro}) \end{cases} \tag{22}$$

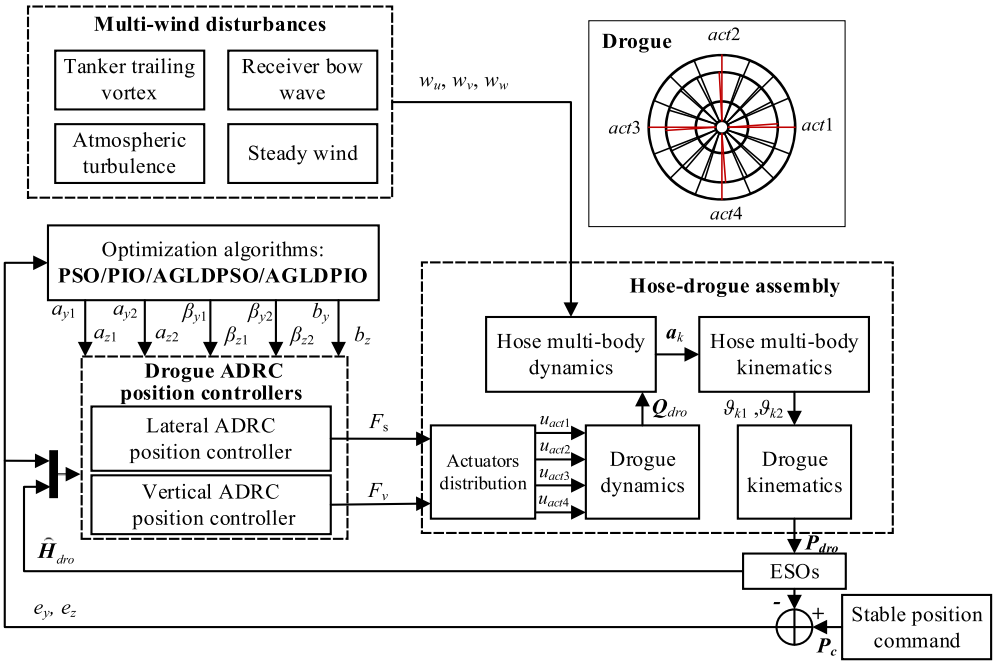

Fig. 3. Architecture of the optimized ADRC position controllers for HDS.

where $\boldsymbol{P}_{dro} \in \mathbb{R}^{2\times1}$, $\widehat{\boldsymbol{P}}_{dro} \in \mathbb{R}^{2\times1}$ denote the real-time values and estimation values of drogue positions in y, z-axes, respectively, $\boldsymbol{P}_{dro} = [y_{dro}, z_{dro}]^T$, $\widehat{\boldsymbol{P}}_{dro} = [\widehat{y}_{dro}, \widehat{z}_{dro}]^T$, $\widehat{\boldsymbol{H}}_{dro} \in \mathbb{R}^{2\times1}$ is the estimation of lumped disturbances, $\widehat{\boldsymbol{H}}_{dro} = [\widehat{h}_{droy}, \widehat{h}_{droz}]^T$, $\boldsymbol{\lambda}_{dro1}$, $\boldsymbol{\lambda}_{dro2}$ are the gain parameters of ESOs, $\boldsymbol{\lambda}_{dro1} = 2\zeta$, $\boldsymbol{\lambda}_{dro2} = \zeta^2$.

Next, to increase the control accuracy and anti-disturbance ability, the integration elements are introduced into the designed ADRC controllers instead of the differentiation elements. Thus, the drogue lateral and vertical ADRC position controllers are developed as

$$\begin{cases} F_s = b_y \cdot \left(\beta_{y1} \cdot \mathrm{fal}(e_y, a_{y1}, \delta_y) + \beta_{y2} \cdot \int \mathrm{fal}(e_y, a_{y2}, \delta_y)\mathrm{d}t - \widehat{h}_{droy} \right) \\ e_y = y_c - \widehat{y}_{dro} \end{cases} \tag{23}$$

$$\begin{cases} F_v = b_z \cdot \left(\beta_{z1} \cdot \mathrm{fal}(e_z, a_{z1}, \delta_z) + \beta_{z2} \cdot \int \mathrm{fal}(e_z, a_{z2}, \delta_z)\mathrm{d}t - \widehat{h}_{droz} \right) \\ e_z = z_c - \widehat{z}_{dro} \end{cases} \tag{24}$$

where e_y, e_z denote the drogue position errors in y, z-axes, respectively, $\boldsymbol{P}_c = [x_c, y_c, z_c]^T$ is the drogue stable position command, b_y, b_z are the disturbance compensation parameters, β_{y1}, β_{z1}, β_{y2}, β_{z2} denote the proportional and integral gains, respectively, a_{y1}, a_{y2}, a_{z1}, a_{z2} are the nonlinear function power, δ_y, δ_z present the width of linear range, $\delta_y = \delta_z$, $\mathrm{fal}(\cdot)$ is a nonlinear function formulated as

$$\mathrm{fal}(e, a, \delta) = \begin{cases} \dfrac{e}{\delta^{1-a}} & |e| \le \delta \\ |e|^a \,\mathrm{sign}(e) & |e| > \delta \end{cases} \tag{25}$$

where $\mathrm{sign}(\cdot)$ is the sign function.

We determine ten parameters need to be optimized for enhancing the drogue controller performance, including a_{y1}, a_{y2}, β_{y1}, β_{y2}, b_y, a_{z1}, a_{z2}, β_{z1}, β_{z2}, b_z. Thus, the dimension of the proposed AGLDPIO algorithm is confirmed as $D = 10$.

4.2. Optimized drogue ADRC position controllers

The proposed optimized ADRC controllers are developed to stabilize the relative position of drogue in the presence of the multi-wind disturbances. As shown in Fig. 3, the architecture of the designed optimized ADRC position controllers for HDS contains the hose-drogue assembly (Section 2), the multi-wind disturbances (Section 2), and the optimized ADRC controllers (Section 3 and 4). Through Section 4.1, we design the lateral and vertical position controllers to obtain the expected active-control aerodynamic forces F_s, F_v. Next, according to the drogue aerodynamic coefficient $\boldsymbol{C}_u$ as described in Section 2.2, the four actuators are distributed to change the relevant opening angles. To be specific, assume that C_u^{ij} denotes the element of matrix $\boldsymbol{C}_u$ at the i-th row and the j-th column, $\boldsymbol{u}_{act}^{ep} \in \mathbb{R}^{4\times1}$ denotes the expected opening angle of actuator, $\boldsymbol{u}_{act}^{ep} = [u_{act1}^{ep}, u_{act2}^{ep}, u_{act3}^{ep}, u_{act4}^{ep}]^T$. The actuator distribution equations are presented as follows:

$$\begin{cases} \Delta u_{act1} = \dfrac{F_s}{2\bar{q}C_u^{21}} \\ \Delta u_{act3} = -\Delta u_{act1} \\ \Delta u_{act1} = u_{act1}^{ep} - u_{act1}^{trim} \\ \Delta u_{act3} = u_{act3}^{ep} - u_{act3}^{trim} \end{cases}, \quad \begin{cases} \Delta u_{act2} = \frac{F_v}{2\bar{q}C_u^{32}} \\ \Delta u_{act4} = -\Delta u_{act2} \\ \Delta u_{act2} = u_{act2}^{ep} - u_{act2}^{trim} \\ \Delta u_{act4} = u_{act4}^{ep} - u_{act4}^{trim} \end{cases} \tag{26}$$

where $\bar{q}$ is the dynamic pressure, $\bar{q} = \frac{1}{2}\rho\|\boldsymbol{V}_{N,air}\|^2$. After $\boldsymbol{u}_{act}^{ep}$ is obtained, the real opening angle $\boldsymbol{u}_{act}$ can be gotten using Eq. (4). Then, the controllable drogue generates the real lateral and vertical active-control aerodynamic forces F_s', F_v'. Then, the different algorithms including AGLDPIO, AGLDPSO, PIO, PSO are implemented to optimize the ten parameters of the designed drogue ADRC controllers for improving the control accuracy, stability, anti-disturbance ability.

The implementation steps of the designed drogue ADRC controllers optimized via AGLDPIO for HDS are presented as follows:

Step 1: Obtain the drogue stable position command. Utilize the hose-drogue assembly and tanker trailing vortex models, and further obtain the drogue initial stable position as the unchanged control command at the end of initial stable time t_{dro}^{ini}.

Step 2: Design the basic lateral and vertical position ADRC controllers and initialize the parameters. As described in Section 4.1, design the basic lateral and vertical ADRC controllers of controllable drogue. Initialize the parameters including the number of pigeon population N_p, the problem dimension D, the map and compass factor R, the ESO gain parameter ζ, etc.

Step 3: Evaluate the fitness values of initial pigeons and obtain the current $\boldsymbol{X}_{gbest}$, $\boldsymbol{X}_{worst}$. Calculate the sum of squares of the drogue's position errors to evaluate the initial parameters of the designed controllers. Through comparing the fitness values, obtain the $\boldsymbol{X}_{gbest}$, $\boldsymbol{X}_{worst}$ at the current generation corresponding to the maximum and minimum fitness values.

Step 4: Select the operator to update the pigeons. Define the maximum update generation $N_{c1\max}$ of the map and compass operator, and the maximum update generation $N_{c2\max}$ of the landmark operator. If $Nc < N_{c1\max}$, conduct the improved map and compass operator, go to **Step 5**. Otherwise, if $0 < Nc - N_{c1\max} < N_{c2\max}$, conduct the landmark operator, go to **Step 6**.

Step 5: Conduct the improved map and compass operator. Determine the subpopulation size M using (19), (20), (21), adaptively. Randomly divide the pigeon population into N_p/M subpopulations (i.e., the slave nodes). For each subpopulation, obtain the $\boldsymbol{X}_w$ and $\boldsymbol{X}_{sbest}$ according to the fitness values. Further, update the velocity and position of the worst pigeon using (17), (18).

Step 6: Conduct the landmark operator. Update the number of pigeons, the center of remaining pigeons, and the positions of pigeons at the current generation using (14), (15), (16).

Step 7: Evaluate the fitness values of pigeons. Carry out the simulation process of the HDS enabling the designed ADRC controllers in the presence of multi-wind disturbances. Then, calculate the sum of squares of position errors in y, z-axes of controllable drogue.

Step 8: Obtain the maximum, minimum fitness values and the global best, worst positions $\boldsymbol{X}_{gbest}$, $\boldsymbol{X}_{worst}$ of pigeons. According to the fitness values of pigeons, determine the global best and worst positions of pigeons. The global best position $\boldsymbol{X}_{gbest}$ of pigeons represents the optimized parameters of the designed ADRC controllers.

Step 9: Terminate and output the final global best position of pigeons. If $Nc > Nc_{1\max} + Nc_{2\max}$, output the final global best position of pigeons as the controllers' optimal parameters. Otherwise, go to **Step 4**.

The detailed flow of AGLDPIO for the optimized ADRC controllers is presented in Fig. 4.

5. Simulation results and analysis

To verify the validity and superiority of the proposed optimized drogue ADRC position controllers, extensive simulation experiments are conducted based on the complex nonlinear model of hose-drogue assembly in the presence of multi-wind disturbances. For comparison, the conventional optimized PID controllers and the proposed optimized ADRC controllers are respectively enabled in the simulation experiments, and different algorithms including PSO, PIO, AGLDPSO, AGLDPIO are utilized to optimize the ten parameters of the designed ADRC controllers. The parameters of simulation experiments are listed in Table 1 and Table 2. The parameters of AGLDPIO, AGLDPSO, PIO, PSO are adopted based on [35], and these specific parameter values are adjusted according to the actual problems. In Table 1, the parameters of the proposed controllers for the optimization process are determined according to the preliminary coarse tuning values and experiences. In Table 2, the simulation parameters are adopted based on [20]. Among them, some parameters are difficult to obtain from the existing references, for example the probe installation position, thus we roughly determine them according to the actual physical cognition.

Case 1. In the simulation experiments of AAR docking, the light turbulence works from 50 s, and the gust is implemented from 80 s. Assume that the tanker takes the fixed straight level flight at the height h, velocity V_T, and the receiver approaches the drogue at the distance d_{R2D}, docking velocity V_{R2T} from 50 s until reaching the drogue stable position command. Besides, the refueling pod is installed

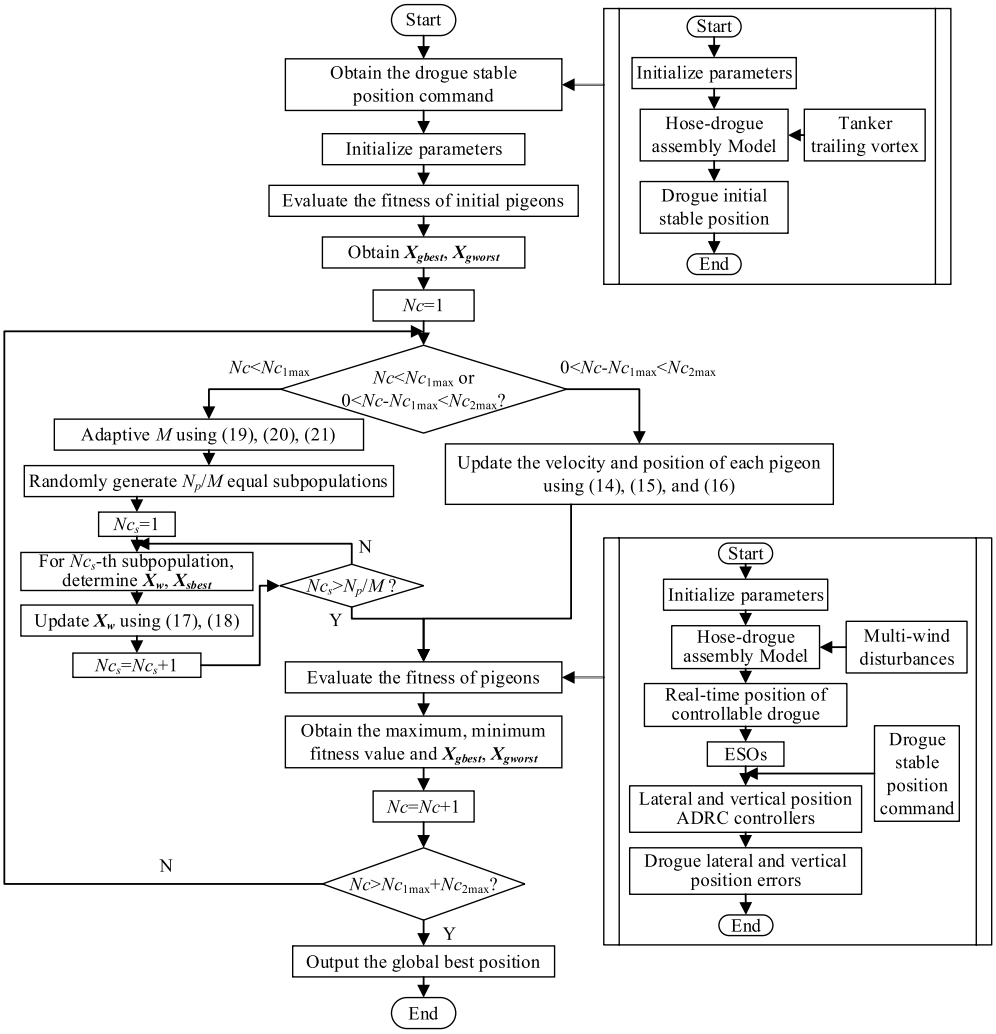

Fig. 4. Detailed flow chart of AGLDPIO for the optimized ADRC controllers.

Table 1
Parameters of AGLDPIO, AGLDPSO, PIO, PSO and controllers.

AGLDPSO, PSO			AGLDPIO, PIO		
Parameter	Description	Value	Parameter	Description	Value
N_s	Number of particles	10	N_p	Number of pigeons	10
$Nc_{\max}$	Max iteration	30	$Nc_{\max}$	Max iteration of two operators	30
c_1	Self acceleration coefficient	0.8	$Nc_{1\max}$	Max iteration of map and compass operator	25
c_2	Global acceleration coefficient	0.5	$Nc_{2\max}$	Max iteration of landmark operator	5
w	Inertia weight	0.5	R	The map and compass factor	0.15
D	Dimension of search space for ADRC controllers	10	D	Dimension of search space for ADRC controllers	10
$M_{\max}$	Max population size of subpopulation	10	$M_{\max}$	Max population size of subpopulation	10
$M_{\min}$	Min population size of subpopulation	2	$M_{\min}$	Min population size of subpopulation	2
n_b	Number of buckets	$0.3Nc_{\max}$	n_b	Number of buckets	$0.3Nc_{\max}$
$a_{ij}^{\max}$	Max nonlinear function power ($i=y,z;\ j=1,2$)	2	$a_{ij}^{\max}$	Max nonlinear function power ($i=y,z;\ j=1,2$)	2
$a_{ij}^{\min}$	Min nonlinear function power ($i=y,z;\ j=1,2$)	0	$a_{ij}^{\min}$	Min nonlinear function power ($i=y,z;\ j=1,2$)	0
β_{ij}^{max}	Max proportional and integral gain ($i=y,z;\ j=1,2$)	10	β_{ij}^{max}	Max proportional and integral gain ($i=y,z;\ j=1,2$)	10
β_{ij}^{min}	Min proportional and integral gain ($i=y,z;\ j=1,2$)	0	β_{ij}^{min}	Min proportional and integral gain ($i=y,z;\ j=1,2$)	0
b_i^{max}	Max disturbance compensation parameter ($i=y,z$)	1000	b_i^{max}	Max disturbance compensation parameter ($i=y,z$)	1000
b_i^{min}	Min disturbance compensation parameter ($i=y,z$)	0	b_i^{min}	Min disturbance compensation parameter ($i=y,z$)	0

Table 2
Other parameters of simulation experiments.

Parameter	Description	Value
t_{simu}	Time of simulation experiments	100 s
V_T	Velocity of tanker	150 m/s
h	Flight height of AAR	7000 m
m_T	Mass of tanker	120000 kg
b_T	Wingspan of tanker	39.88 m
L	Hose total length	22.86 m
N_{hose}	Number of hose links	24
m_{dro}	Mass of controllable drogue	29.5 kg
d_{dro}	Drogue diameter	0.61 m
c_{dro}	Aerodynamic force coefficient of drogue	0.831
V_{R2T}	Receiver docking velocity	1.5 m/s
d_{R2D}	Distance of receiver behind drogue	25 m
d_{pod}	Refueling pod installation position relative to right wingtip	2.85 m
$(gust_u\ gust_v\ gust_w)$	Velocity of gust	$\begin{pmatrix} 0 & -6 & 4 \end{pmatrix}$ m/s
$\begin{pmatrix} d_x & 0 & d_z \end{pmatrix}$	Offset value between $O_{TV}X_{TV}Y_{TV}Z_{TV}$ and $O_{TB}X_{TB}Y_{TB}Z_{TB}$	$\begin{pmatrix} 2 & 0 & 2 \end{pmatrix}$ m
h_{nose}	Maximum radius of receiver nose in width direction	0.4 m
$\boldsymbol{P}_{probe}$	Position of the probe in receiver nose coordinate frame	$\begin{pmatrix} -2.05 & 0.5 & -0.86 \end{pmatrix}$ m
U	Averaged flow velocity	V_T m/s
$\boldsymbol{u}_0$	Trim opening angle of actuator	[30.24° 30.24° 30.24° 30.24°]
$\boldsymbol{C}_u$	Drogue opening angular aerodynamic coefficient	$\begin{bmatrix} -8.64 & -10.41 & -8.64 & -3.44 \\ -56.4 & 0 & 56.4 & 0 \\ -3.44 & -53.4 & -3.44 & 53.4 \end{bmatrix} \times 10^{-4}$ m^2/°

Table 3
Drogue position statistical property (80 s-100 s).

		50 s	100 s	Max-Min	Mean	Std
Without control	x (m)	−21.30	−21.60	0.32	−21.50	0.0765
	y (m)	18.06	17.73	2.44	17.23	0.6781
	z (m)	8.05	7.25	1.07	7.55	0.2407
Optimized PID	x (m)	−21.30	−21.31	0.046	−21.32	0.0097
	y (m)	18.06	18.08	0.120	18.05	0.0300
	z (m)	8.05	8.07	0.112	8.05	0.0232
Optimized ADRC	x (m)	−21.30	−21.32	0.029	−21.32	0.0063
	y (m)	18.06	18.06	0.037	18.06	0.0050
	z (m)	8.05	8.05	0.030	8.05	0.0050

around the tanker right wingtip, and we give the initial states of hose-drogue assembly as $\vartheta_{k1} = 30°, \vartheta_{k2} = 0°, \dot{\vartheta}_{k1} = 0, \dot{\vartheta}_{k2} = 0$. To indicate the essential characteristics of HDS, the drogue position controllers are disabled in this case.

In Fig. 5, the states of hose-drogue assembly at different times effectively reflect the flexibility of HDS in the presence of multi-wind disturbances. As shown in Fig. 6(b)-(d), the hose-drogue assembly gradually stabilizes to the initial stable position in the first 50 s under the influence of the steady flowfield (i.e., the free stream and tanker trailing vortex). The initial stable position at 50 s can be regarded as the unchanged position control command of the designed controllers as listed in Table 3. In Fig. 6(a), it is obvious that there are two relatively stable regions of the drogue motion trajectory. The drogue moves from the initial stable position to the final swing region along with the multi-wind disturbances acting from 50 s. Noting that the size of final swing region is about 1.2 m × 2.5 m, but the effective capture radius R_c [40] is defined as 0.1 m inside the outer ring of drogue, i.e., $R_c = 0.205$ m. Thus, it is extremely difficult to guarantee the success rate of AAR docking through holding the drogue swinging in the region of radius R_c. Further, we can see from Fig. 6(b)-(d) and Table 3 that the *Max-Min* values of drogue position in x, y, z-axes are 0.32 m, 2.44 m, 1.07 m, respectively, which are much larger than $2R_c = 0.41$ m. Moreover, when compare the drogue positions at 50 s and 100 s, there exists an obvious position offset due to the influence of multi-wind disturbances. Besides, the receiver might be trapped into the problem of chasing the drogue in that the drogue position changes in high-frequency quick speed, which could cause the AAR accidents, such as the hose whipping, probe fracture, drogue fracture, etc.

Case 2. The simulation conditions are the same as Case 1. In this case, the optimized PID and ADRC position controllers of drogue are enabled from 50 s, respectively.

In Case 2, we enable the optimized ADRC position controllers to stabilize the position of drogue in the presence of multi-wind disturbances, which demonstrates the effectiveness and superiority of the designed controllers. Through utilizing the AGLDPIO algorithm to

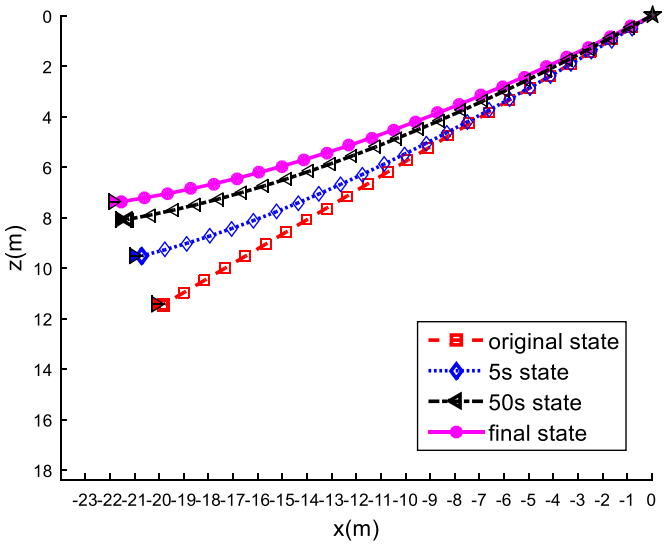

Fig. 5. States of hose-drogue assembly in Case 1.

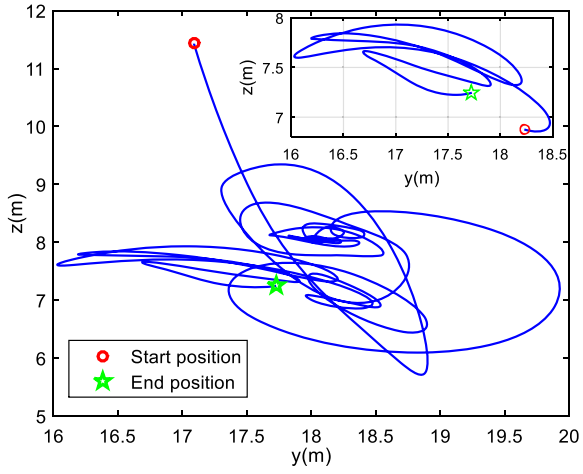

(a) Drogue motion trajectory in $O_{hd}Y_{hd}Z_{hd}$

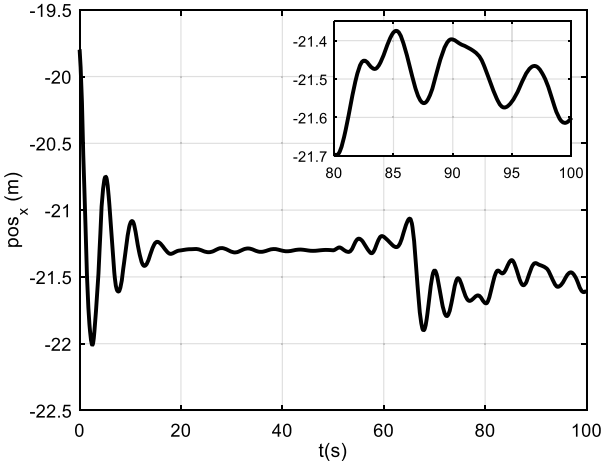

(b) Drogue positions in x-axis

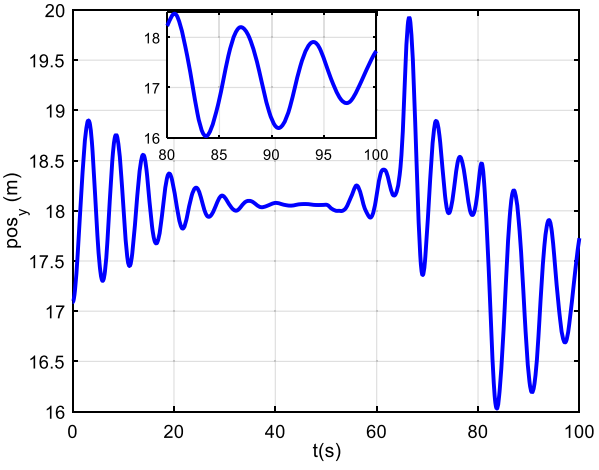

(c) Drogue positions in y-axis

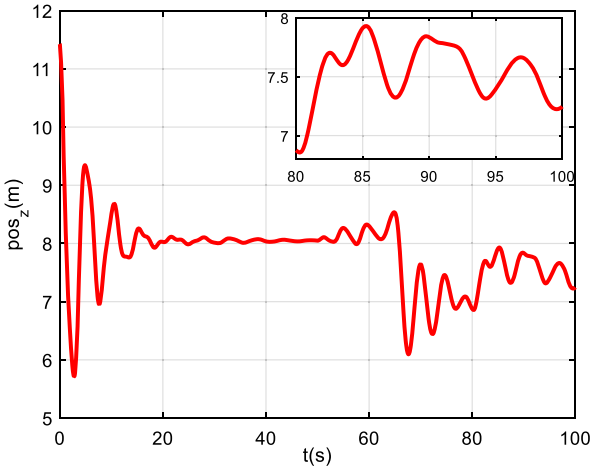

(d) Drogue positions in z-axis

Fig. 6. Simulation results of drogue position in Case 1.

Table 4
Parameters of the PID and ADRC controllers optimized by AGLDPIO.

Controller	Parameters	Value
PID	$[k_P^s, k_I^s, k_D^s, k_P^y, k_I^y, k_D^y]$	[719.2042, 296.6488, 367.6559, 485.3442, 615.0032, 450.7548]
ADRC	$[a_{y1}, a_{y2}, \beta_{y1}, \beta_{y2}, b_y, a_{z1}, a_{z2}, \beta_{z1}, \beta_{z2}, b_z]$	[1.1226, 0.6026, 5.6387, 8.8240, 464.4901, 1.2744, 0.5914, 1.9020, 7.6329, 858.5174]

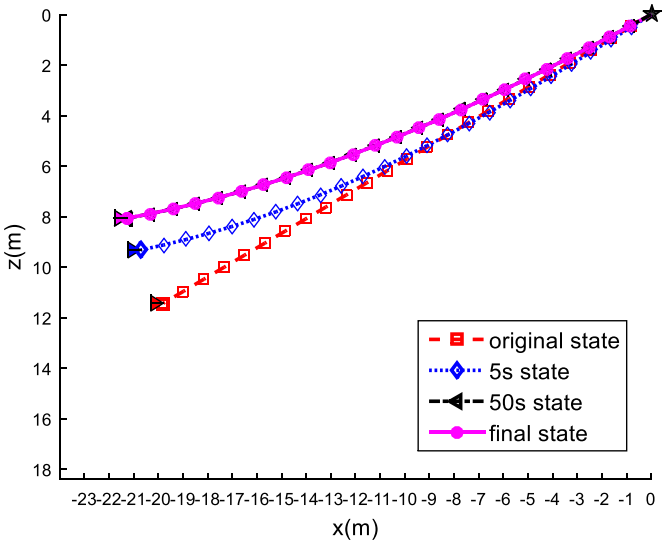

Fig. 7. States of hose-drogue assembly with optimized ADRC controllers in Case 2.

optimize the PID and ADRC position controllers, the optimized parameters of the designed controllers can be obtained as listed in Table 4. We can clearly see from Fig. 7 that the final state of hose-drogue assembly is basically coincident with the 50 s state, which indicates that the optimized ADRC controllers commendably stabilize the drogue position under the influence of multi-wind disturbances. When compare the drogue motion trajectories presented in Fig. 8(a) and Fig. 6(a), there is a significant reduction in the range of drogue swing region, from 1.2 m × 1.5 m to 0.04 m × 0.04 m. Thus, it can be concluded that the swing range of drogue meets the requirement of the effective capture radius R_c while the optimized ADRC position controllers are enabled. Besides, because the final position of drogue changes slightly with respect to the initial stable position, the AAR dynamic docking process can be regraded as a process where the receiver attempts to dock into the predetermined fixed position of drogue. Further, as shown in Fig. 8(b)-(d), we evaluate the control effects of the optimized PID and ADRC controllers by comparing the simulation results of drogue positions in 64 s-69 s and 80 s-100 s. In 64 s-69 s, the designed optimized ADRC controllers maintain the drogue position with a smaller position error than the optimized PID controllers. It can be seen from Fig. 9 that the position jitter of drogue in 64 s-69 s is caused by the abrupt dramatical change of receiver bow wave. Thus, we can draw the conclusion that the designed optimized ADRC controllers possess the better ability to resist the abrupt dramatical change of disturbances. In 80 s-100 s, compared with the PID controllers, our proposed controllers hold the drogue in a smaller swing range, which represents the better ability to resist the high-frequency atmospheric turbulence. Table 3 gives the drogue position statistical property in 80 s-100 s for quantitative analysis. It is obvious that the swing range (*Max-Min*), mean position offset (*Mean*-50 s state) and standard deviation (*Std*) are significantly reduced when we enable the optimized position controllers (PID or ADRC). Among the two control methods, our proposed ADRC controllers perform better in terms of the swing range and standard deviation of drogue position. As listed in Table 3, the *Max-Min* values of the optimized ADRC controllers decrease from 0.046 m to 0.029 m in x-axis, from 0.120 m to 0.037 m in y-axis, from 0.112 m to 0.030 m in z-axis. Besides, the standard deviation values of the optimized ADRC controllers only occupy less than a quarter of those of the optimized PID controllers in y, z-axes. Therefore, our proposed optimized ADRC position controllers are more superior in anti-disturbance ability and position stability, which reduces the difficulties of AAR docking and guarantees the docking success rate.

As shown in Fig. 9, the velocities of the multi-wind disturbances in Case 2 change a lot in the AAR docking. We can see from Fig. 9(a) that the velocity of tanker trailing vortex gradually approaches the stable value. In Fig. 9(b), the velocity of receiver bow wave exists an abrupt dramatical change in 64 s-69 s in that the probe arrives around the docking position. Fig. 9(d) presents the resultant velocities of the multi-wind disturbances which change in the range about 20 m/s in x, y, z-axes. The real lateral and vertical active-control aerodynamic forces are illustrated in Fig. 10. It is obvious that the optimized ADRC position controllers generate the larger active-control forces in the abrupt changing points of multi-wind disturbances, and the high-frequency active-control forces are produced by the optimized ADRC position controllers to resist the atmospheric turbulence. In Fig. 11, the corresponding opening angles of four actuators are limited in the normal range less than 4 degrees.

Four algorithms (PSO/PIO/AGLDPSO/AGLDPIO) are implemented to optimize the ADRC position controllers in independent 10 times for effectiveness evaluation of these algorithms. The evolution curves and the optimized ADRC position controller parameters of four algorithms are presented in Fig. 12 and Table 5. Among the four algorithms, our proposed AGLDPIO algorithm acquires the minimum fitness value beginning with the almost same initial value. The minimum fitness value denotes that the ADRC position controllers optimized via AGLDPIO stabilize the drogue to the minimum position error, which means the best anti-disturbance ability and position stability. Further, through analyzing the evolution curves of the designed ADRC controllers, we can obtain the following conclusions:

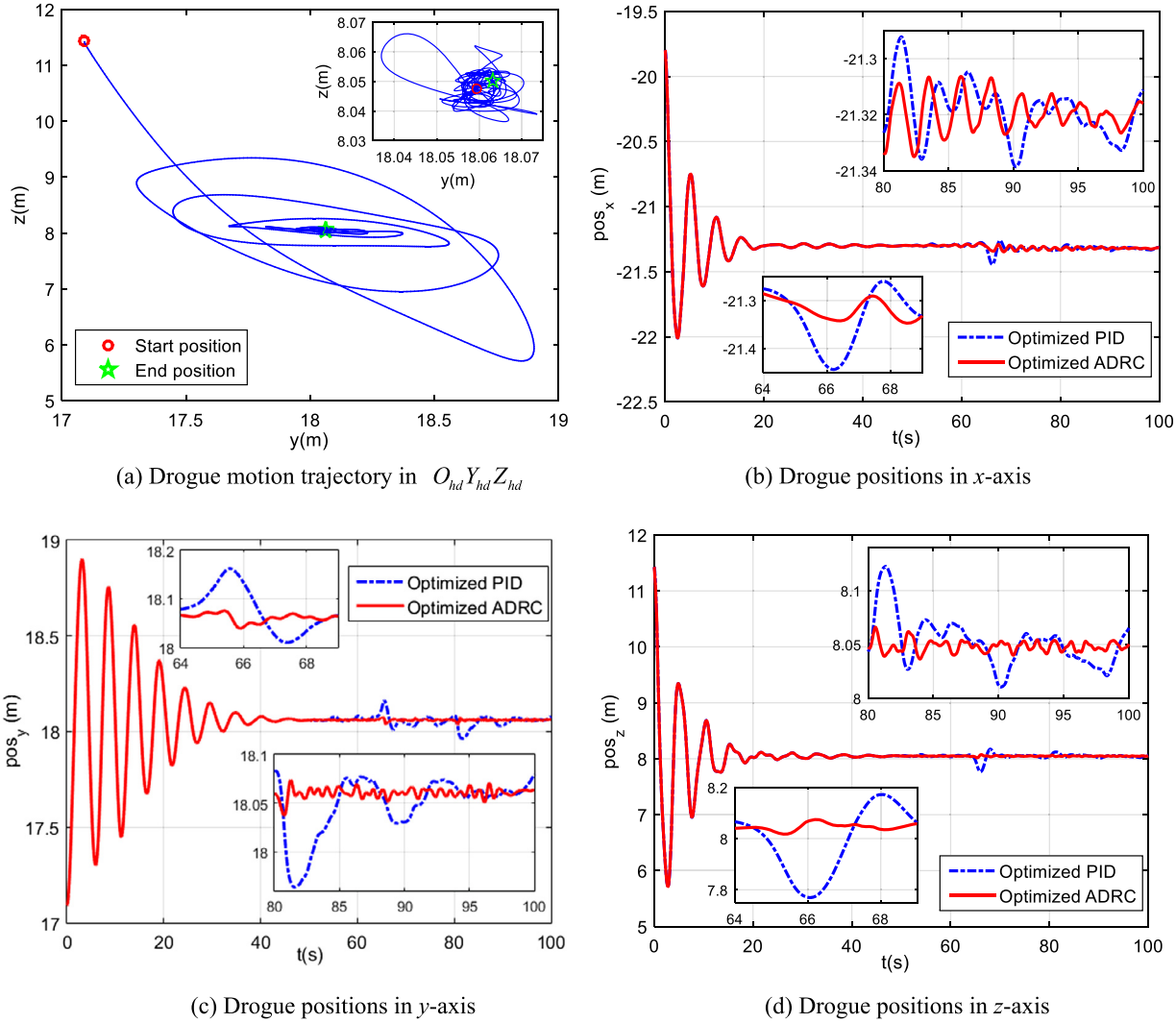

(a) Drogue motion trajectory in $O_{hd}Y_{hd}Z_{hd}$

(b) Drogue positions in x-axis

(c) Drogue positions in y-axis

(d) Drogue positions in z-axis

Fig. 8. Simulation results of drogue position in Case 2.

Table 5
Optimized ADRC position controller parameters of four algorithms.

Algorithm	Controller parameters $[a_{y1}, a_{y2}, \beta_{y1}, \beta_{y2}, b_y, a_{z1}, a_{z2}, \beta_{z1}, \beta_{z2}, b_z]$	Fitness
AGLDPIO	[1.1226, 0.6026, 5.6387, 8.8240, 464.4901, 1.2744, 0.5914, 1.9020, 7.6329, 858.5174]	19.6171
AGLDPSO	[0.9210, 1.0622, 4.6359, 4.8889, 500.2871, 0.7593, 0.9050, 3.2884, 4.0626, 613.5766]	26.3173
PIO	[1.0119, 0.5976, 5.7221, 4.2199, 484.7846, 0.3860, 0.3539, 1.1610, 4.2036, 564.5297]	29.3068
PSO	[0.9776, 0.4652, 6.2903, 2.7301, 402.1154, 0.4111, 0.4611, 1.5556, 3.0073, 538.5271]	33.4724

(1) As shown in Fig. 12, the PIO algorithm converges fastest among the other algorithms, which means that the map and compass operator can best refine the promising solutions in the search space to optimize the ADRC controller parameters. Because it can be seen from equation (12) that the velocity of the PIO algorithm is depended on the rapidly descending negative exponential residue and only using the global best position. Thus, the PIO algorithm can easily fall into the local optimal solutions.

(2) Through importing the adaptive granularity learning strategy, the AGLDPSO and AGLDPIO algorithms enhance the exploration ability at the late generations by adaptively adjusting the subpopulation size. As a sacrifice, the improved algorithms slightly reduce the convergence rate at the early generations.

6. Conclusions

In this paper, we propose an optimized ADRC position control method to stabilize the drogue position for resisting the multi-wind disturbances. First, the hose-drogue assembly is modeled as a link-connected system with a controllable drogue using the finite-segment multi-body method, which reflects the flexibility of hose. The AAR atmospheric flow environment is constructed by importing the multi-wind disturbance models. Then, we develop an improved PIO algorithm, called as AGLDPIO, to balance the exploration and exploitation abilities by adaptively adjusting the subpopulation size for obtaining the global optimal solution. Moreover, the drogue ADRC position controllers optimized via AGLDPIO are designed to reduce the position swing range of drogue in the presence of multi-wind disturbances.

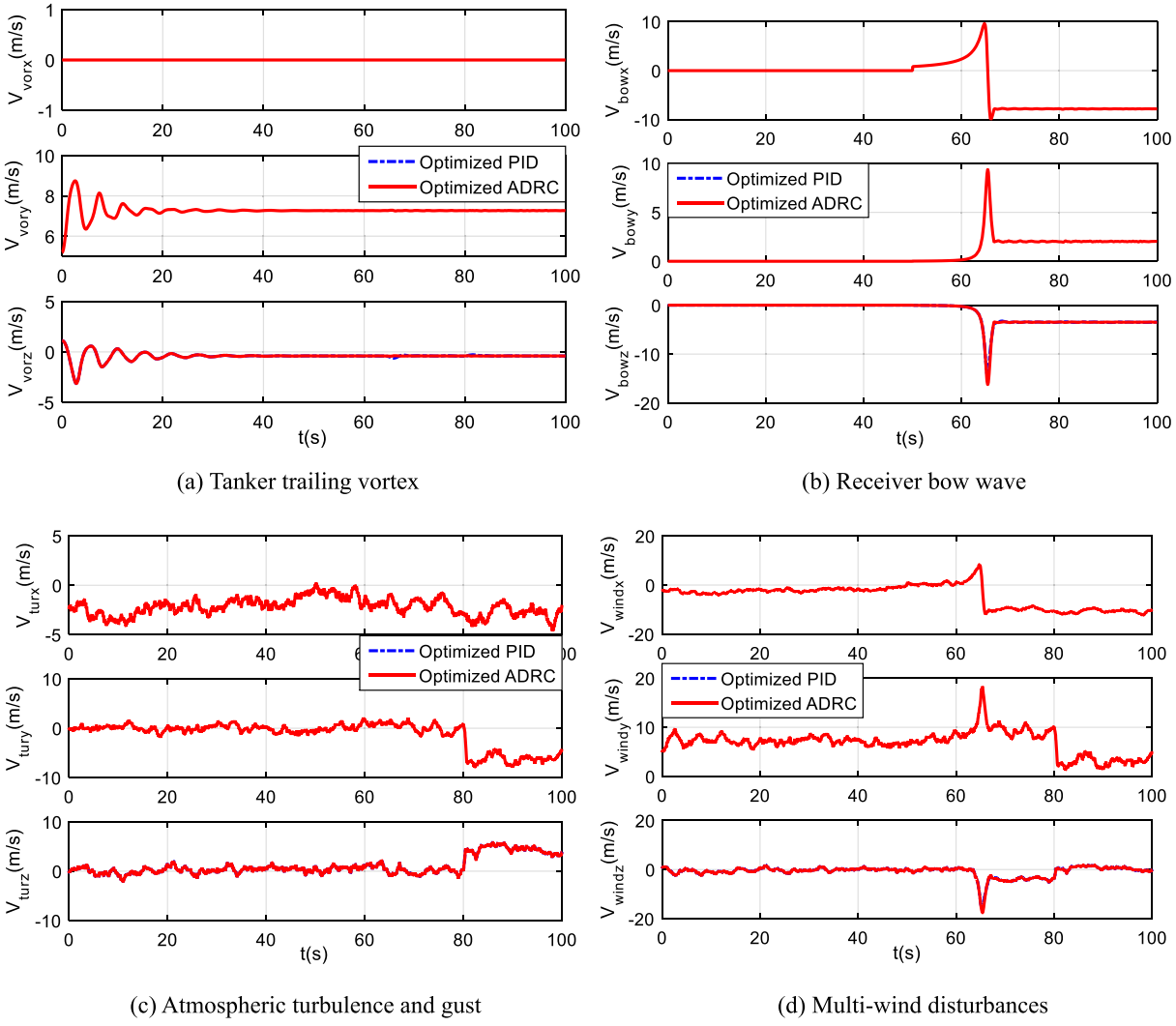

Fig. 9. Velocities of multi-wind disturbances in Case 2.

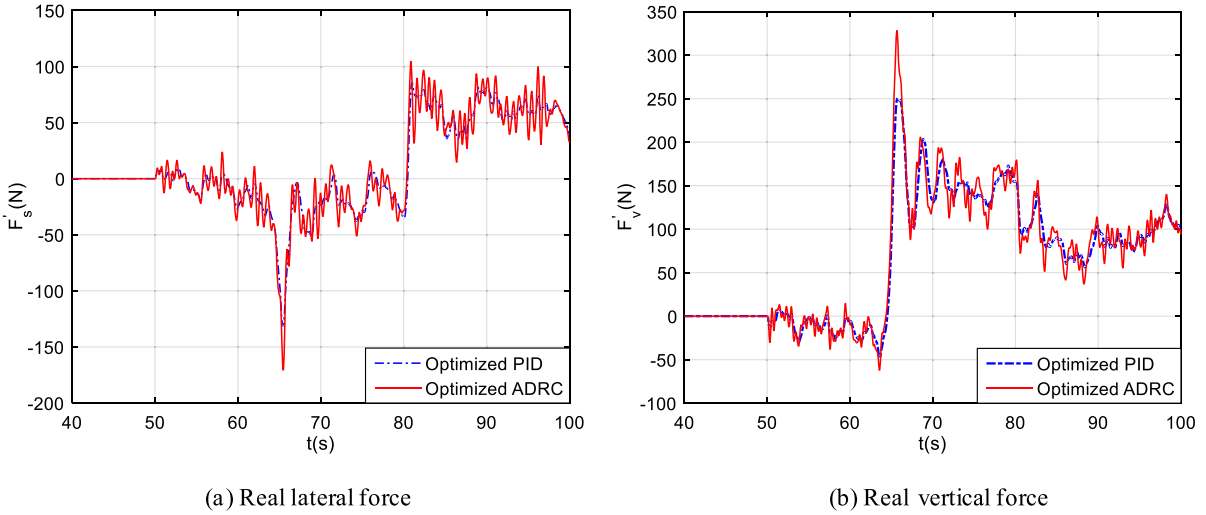

Fig. 10. Real lateral and vertical active-control aerodynamic forces in Case 2.

The simulation results indicate that our proposed ADRC position controllers can stabilize the drogue to swing in a smaller range satisfying the effective capture criterion, which demonstrates the effectiveness and superiority of the proposed controllers in anti-disturbance ability and position stability. In the future, we will focus on the application of our proposed control method combining the ground semi-physical AAR experiment platform.

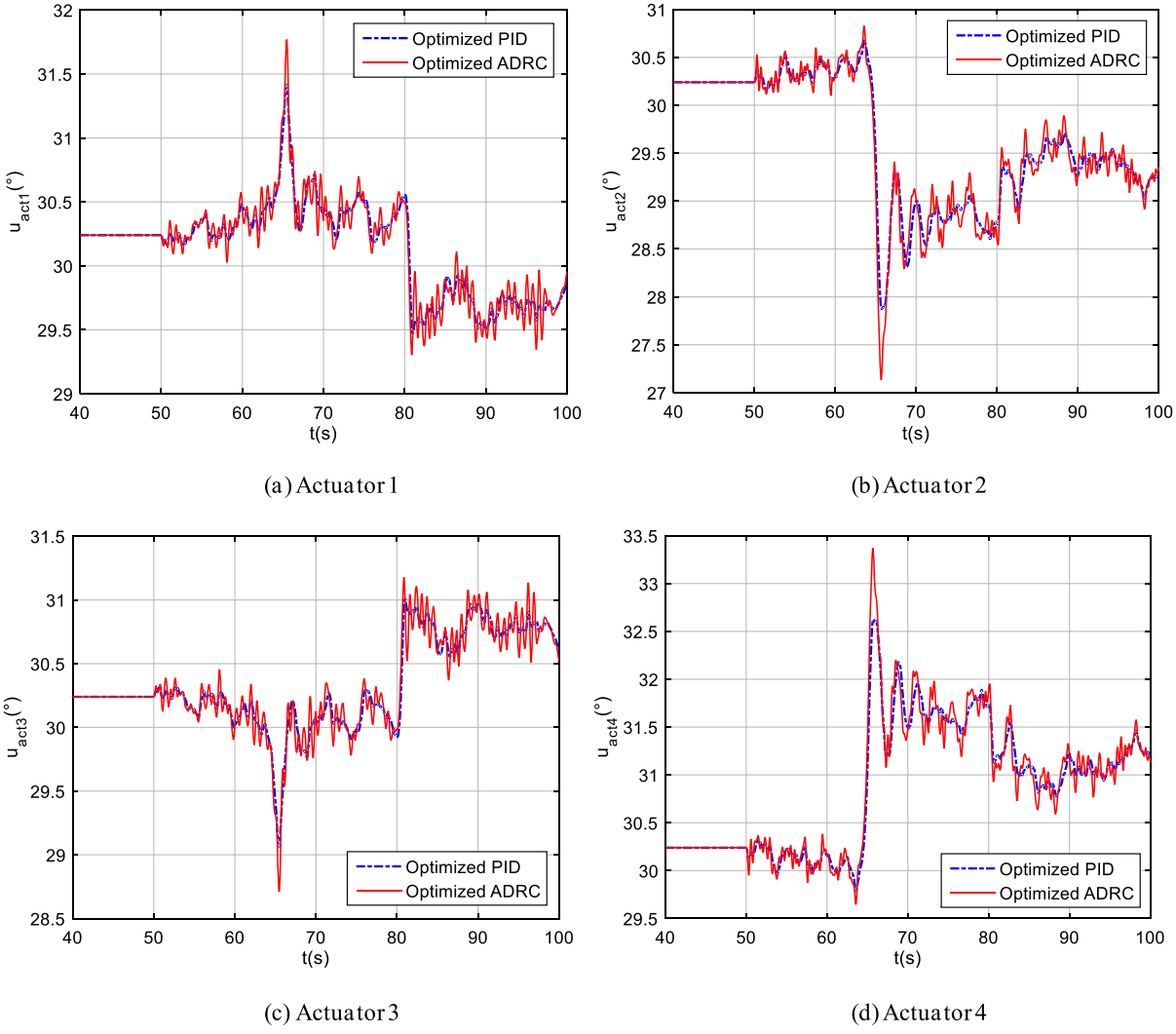

Fig. 11. Opening angles of four actuators.

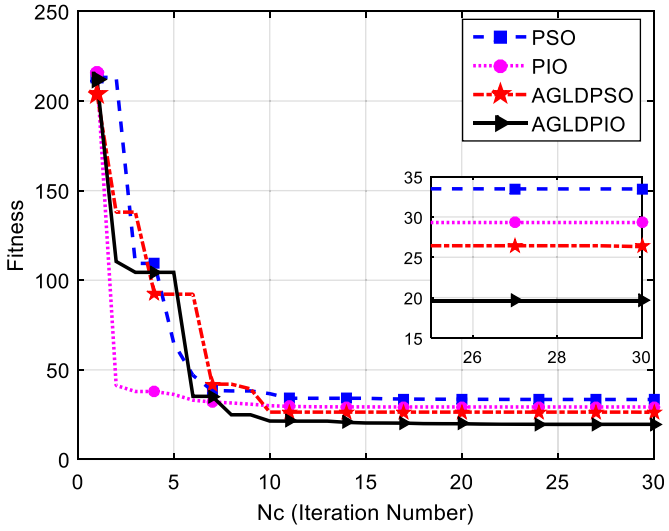

Fig. 12. Evolution curves of four algorithms for designed ADRC controllers.

Declaration of competing interest

The authors declare the following financial interests/personal relationships which may be considered as potential competing interests: Yongbin Sun reports financial support was provided by National Natural Science Foundation of China. Yongbin Sun reports financial support

was provided by China Postdoctoral Science Foundation. Zhijie Liu reports financial support was provided by Guangdong Basic and Applied Basic Research Foundation. Xiuyu He reports financial support was provided by National Natural Science Foundation of China.

Acknowledgements

This work was supported in part by the National Natural Science Foundation of China under Grant 62103040, Grant 62103414, and Grant U2013201, in part by the China Postdoctoral Science Foundation under Grant 2021M690357, and in part by the Guangdong Basic and Applied Basic Research Foundation under Grant 2019A1515110728.

References

[1] K. Eilker, S. Grouni, M. Tadjine, et al., Practical finite time adaptive robust flight control system for quad-copter UAVs, Aerosp. Sci. Technol. 98 (2020) 105708.
[2] Z.Y. Zhen, G. Tao, Y. Xu, et al., Multivariable adaptive control based consensus flight control system for UAVs formation, Aerosp. Sci. Technol. 93 (2019) 105336.
[3] P. Li, H.B. Duan, A potential game approach to multiple UAV cooperative search and surveillance, Aerosp. Sci. Technol. 68 (2017) 403–415.
[4] H. Xiao, R.X. Cui, D.M. Xu, A sampling-based Bayesian approach for cooperative multiagent online search with resource constraints, IEEE Trans. Cybern. 48 (6) (2018) 1773–1785.
[5] N. Nigam, S. Bieniawski, I. Kroo, et al., Control of multiple UAVs for persistent surveillance: algorithm and flight test results, IEEE Trans. Control Syst. Technol. 20 (5) (2012) 1236–1251.
[6] A. Das, S. Shirazipourazad, D. Hay, et al., Tracking of multiple targets using optimal number of UAVs, IEEE Trans. Aerosp. Electron. Syst. 55 (4) (2019) 1769–1784.
[7] H.B. Duan, J.X. Zhao, Y.M. Deng, et al., Dynamic discrete pigeon-inspired optimization for multi-UAV cooperative search-attack mission planning, IEEE Trans. Aerosp. Electron. Syst. 57 (1) (2021) 706–720.
[8] P.R. Thomas, U. Bhandari, S. Bullock, et al., Advances in air to air refueling, Prog. Aerosp. Sci. 71 (2014) 14–35.
[9] Y.B. Sun, Y.M. Deng, H.B. Duan, et al., Bionic visual close-range navigation control system for the docking stage of probe-and-drogue autonomous aerial refueling, Aerosp. Sci. Technol. 91 (2019) 139–149.
[10] S.A. Cambone, K. Krieg, P. Pace, et al., Unmanned Aircraft Systems Roadmap 2005-2030, Office of the Secretary of Defense, 8 2005, pp. 4–15.
[11] J.P. Nalepka, J.L. Hinchman, Automated aerial refueling: extending the effectiveness of unmanned air vehicles, in: AIAA Modeling and Simulation Technologies Conference and Exhibit, San Francisco, California, 2005, AIAA 2005-6005.
[12] H.B. Duan, Y.B. Sun, Y.H. Shi, Bionic visual control for probe-and-drogue autonomous aerial refueling, IEEE Trans. Aerosp. Electron. Syst. 57 (2) (2021) 848–865.
[13] Q. Quan, Z.B. Wei, J. Gao, et al., A survey on modeling and control problems for probe and drogue autonomous aerial refueling at docking stage, Acta Aeronaut. Astronaut. Sin. 35 (9) (2014) 2390–2410.
[14] M.J. Vachon, R.J. Ray, Calculated drag of an aerial refueling assembly through airplane performance analysis, in: 42nd AIAA Aerospace Sciences Meeting and Exhibit, Reno, Nevada, 2004, AIAA 2004-381.
[15] J.L. Hansen, J.E. Murray, N.V. Campos, The NASA Dryden flight test approach to an aerial refueling system, NASA Dryden Flight Research Center, 2005, Report No.: NASA/TM-2005-212859.
[16] J.C. Vassberg, D.T. Yeh, A.J. Blair, et al., Dynamic characteristics of a KC-10 wing-pod refueling hose by numerical simulation, in: 20th Applied Aerodynamics Conference, St. Louis, Missouri, 2002, AIAA 2002-2712.
[17] Z.H. Zhu, S.A. Meguid, Modeling and simulation of aerial refueling by finite element method, Int. J. Solids Struct. 44 (2007) 8057–8073.
[18] K. Ro, J.W. Kamman, Modeling and simulation of hose-paradrogue aerial refueling systems, J. Guid. Control Dyn. 33 (1) (2010) 53–63.
[19] W.R. Williamson, G.J. Glenn, S.M. Stecko, et al., Controllable drogue for automated aerial refueling, J. Aircr. 47 (2) (2010) 515–527.
[20] H.T. Wang, X.M. Dong, J.P. Xue, et al., Dynamic modeling of a hose-drogue aerial refueling system and integral sliding mode backstepping control for the hose whipping phenomenon, Chin. J. Aeronaut. 27 (4) (2014) 930–946.
[21] Z.J. Liu, J.K. Liu, W. He, Modeling and vibration control of a flexible aerial refueling hose with variable lengths and input constraint, Automatica 77 (2017) 302–310.
[22] Z.J. Liu, X.Y. He, Z.J. Zhao, et al., Vibration control for spatial aerial refueling hoses with bounded actuators, IEEE Trans. Ind. Electron. 68 (5) (2021) 4209–4217.
[23] K. Ro, T. Kuk, J.W. Kamman, Active control of aerial refueling hose-drogue systems, in: AIAA Guidance, and Control Conference, Toronto, Ontario Canada, 2010, AIAA 2010-8400.
[24] S.C. Kriel, J.A.A. Engelbrecht, T. Jones, Receptacle normal position control for automated aerial refueling, Aerosp. Sci. Technol. 29 (1) (2013) 296–304.
[25] P.R. Thmoas, S. Bullock, T.S. Richardson, et al., Collaborative control in a flying-boom aerial refueling simulation, J. Guid. Control Dyn. 38 (7) (2015) 1274–1289.
[26] Y.B. Sun, H.B. Duan, N. Xian, Fractional-order controllers optimized via heterogeneous comprehensive learning pigeon-inspired optimization for autonomous aerial refueling hose-drogue system, Aerosp. Sci. Technol. 81 (2018) 1–13.
[27] P. Riccardo, J. Kennedy, T. Blackwell, Particle swarm optimization, Swarm Intell. 1 (1) (2007) 33–57.
[28] H.B. Duan, X.Y. Zhang, J. Wu, et al., Max-min adaptive ant colony optimization approach to multi-UAVs coordinated trajectory re-planning in dynamic and uncertain environments, J. Bionics Eng. 6 (2) (2009) 161–173.
[29] H. Wang, W.J. Wang, S.Y. Xiao, et al., Improving artificial bee colony algorithm using a new neighborhood selection mechanism, Inf. Sci. 527 (2020) 227–240.
[30] L.B. Ma, S. Cheng, Y.H. Shi, Enhancing learning efficiency of brain storm optimization via orthogonal learning design, IEEE Trans. Syst. Man Cybern. Syst. (2020), https://doi.org/10.1109/TSMC.2020.2963943.
[31] H.B. Duan, P.X. Qiao, Pigeon-inspired optimization: a new swarm intelligence optimizer for air robot path planning, Int. J. Intell. Comput. Cybern. 7 (1) (2014) 24–37.
[32] C. Li, H.B. Duan, Target detection approach for UAVs via improved pigeon-inspired optimization and edge potential function, Aerosp. Sci. Technol. 39 (2014) 352–360.
[33] W.Y. Ruan, H.B. Duan, Multiple UAVs obstacle avoidance control via multi-objective social learning pigeon-inspired optimization, Front. Inf. Tech. Electr. Eng. 21 (5) (2020) 740–748.
[34] H. Alazzam, A. Sharieh, K.E. Sabri, A feature selection algorithm for intrusion detection system based on pigeon inspired optimizer, Expert Syst. Appl. 148 (2020) 113249.
[35] Z.J. Wang, Z.H. Zhan, S. Kwong, et al., Adaptive granularity learning distributed particle swarm optimization for large-scale optimization, IEEE Trans. Cybern. 51 (3) (2021) 1175–1188.
[36] S. Venkataramanan, A. Dogan, Modeling of aerodynamic coupling between aircraft in close proximities, in: AIAA Atmospheric Flight Mechanics Conference and Exhibit, Providence, Rhode Island, 2004, AIAA-2004-5172.
[37] U. Bhandari, P.R. Thomas, S. Bullock, et al., Bow wave effect in probe and drogue aerial refuelling, in: AIAA Guidance, Navigation, and Control, (GNC) Conference, Boston, MA, 2013, AIAA-2013-4695.
[38] S. Gage, Creating a unified graphical wind turbulence model from multiple specifications, in: AIAA Modeling and Simulation Technologies Conference and Exhibit, Austin, Texas, 2003, AIAA 2003-5529.
[39] J.Q. Han, From PID to active disturbance rejection control, IEEE Trans. Ind. Electron. 56 (3) (2009) 900–906.
[40] R.P. Dibley, M.J. Allen, Autonomous airborne refueling demonstration phase I flight-test results, in: AIAA Atmospheric Flight Mechanics Conference and Exhibit, Hilton Head, South Carolina, 2007, AIAA 2007-6639.